Electronic Supplementary Material (ESI) for Physical Chemistry Chemical Physics.

SUPPORTING INFORMATION

Mechanistic insight into oxygen vacancy migration in $SrFeO_{3-\delta}$ from DFT+*U* simulations

Musa Alaydrus,*[a] Ikutaro Hamada [a,b] and Yoshitada Morikawa*[a,b,c]

[a] Department of Precision Engineering, Graduate School of Engineering, Osaka University, 2-1 Yamadaoka, Suita, Osaka 565-0871, Japan

[b] Element Strategy Initiative for Catalysis and Batteries, Kyoto University, Goryo-Ohara, Nishikyo-ku, Kyoto 615-8520, Japan

[c] Research Center for Precision Engineering, Graduate School of Engineering, Osaka University, Suita, Osaka 565-0871, Japan

S1: Tuning GGA+U

In this work, the U value was obtained by fitting to the experimental Fe oxides formation enthalpy, where correction to O_2 molecule binding energy error is taken into account, as proposed by Wang *et al.*[1] First, the correction for the O_2 binding energy errors is determined by fitting the experimental formation enthalpy and calculated oxide formation energies,

$$M + \frac{x}{2} O_2 \rightarrow MO_x. \qquad \text{(S1)}$$

Fig. S1 (left) shows the enthalpy to form various oxides from their metals as calculated GGA. In this work, we obtained $\Delta H(O_2)$ = -1.32 eV/O_2 as a correction. The obtained correction, as have been discussed by Lee *et al.*,[2] is dependent on the specific choice of exchange-correlation approximation and pseudopotential. The oxidation reaction energies of the reaction

$$MO_x + \frac{y-x}{2} O_2 \rightarrow MO_y, \qquad \text{(S2)}$$

are calculated as

$$\Delta H(O_2) = \frac{E\left(MO_y\right) - E(MO_x) - \frac{y-x}{2} E(O_2)}{\frac{y-x}{2}}. \qquad \text{(S3)}$$

Experimental formation enthalpy of compounds at room temperature was obtained from the JANAF thermochemical tables.[3] Fig. S1 (right) shows the comparison of the experimental and calculated oxidation energies of Fe_2O_3 (i.e. 4FeO + O_2 → $2Fe_2O_3$) and Fe_3O_4 (i.e. 6FeO + O_2 → $2Fe_3O_4$). $\Delta H(O_2)$ correction is taken into account to obtain these results. Figures S2 and S3 show how the energetics, lattice parameters, and magnetic ordering behave as functions of applied U values and compared with the experiments, whenever available. Small U_{eff} values result in better agreement with the experimental lattice parameters (Fig. S2a) and Fe magnetic moment (Fig. S2b), while larger U_{eff} values give better description in terms of energetics (Fig. S2c and S2d). Therefore, in this work, we applied U_{eff} = 4 eV, together with the oxygen molecule binding energy correction $\Delta H(O_2)$, to study the reaction energetics and V_O migration energies in $SrFeO_{3-\delta}$.

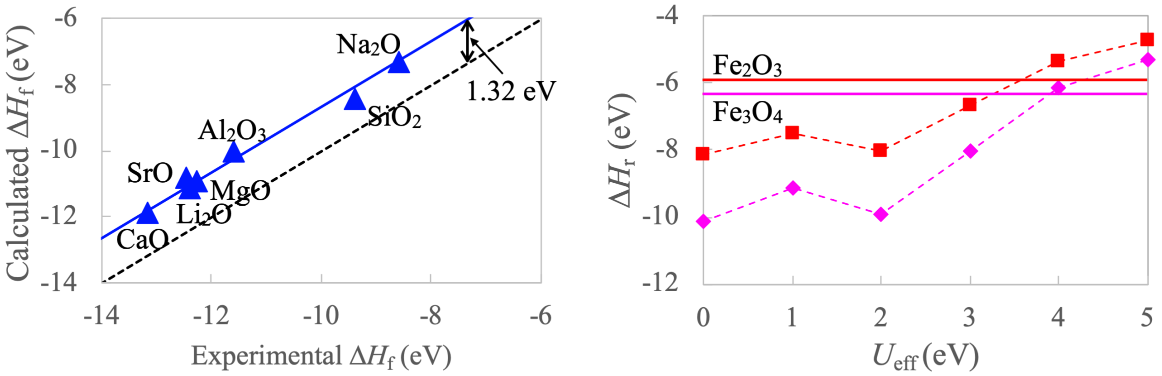

FIG. S1. (Left) Calculated formation energies per O_2 molecule (solid line) of non-transition metal oxides (CaO, SrO, MgO, Li_2O, Al_2O_3, SiO_2, and Na_2O) as function of the experimental formation enthalpies obtained from ref. [2]. (Right) Oxidation energies of Fe_2O_3 and Fe_3O_4 as functions of U_{eff} value and comparison with the experimental value (solid lines).[2]

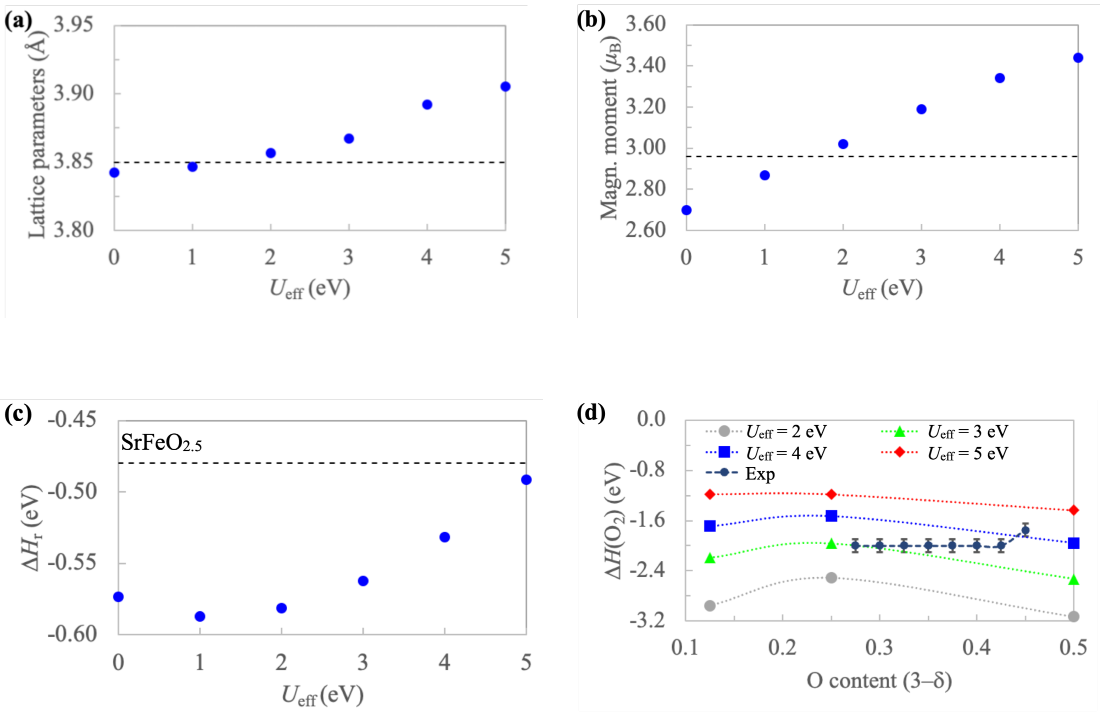

FIG. S2. Lattice parameters (a) and magnetic moment (b) of cubic SrFeO$_3$ as functions of U_{eff} value and comparison with experiments.[4,5] (c) Heat of formation of brownmillerite SrFeO$_{2.5}$ (i.e. SrO + 1/2Fe$_2$O$_3$ → SrFeO$_{2.5}$) as a function of U_{eff} value and comparison with the experiment.[6] (d) Oxygen reaction enthalpy with various U_{eff} values and comparison to the experiment.[7]

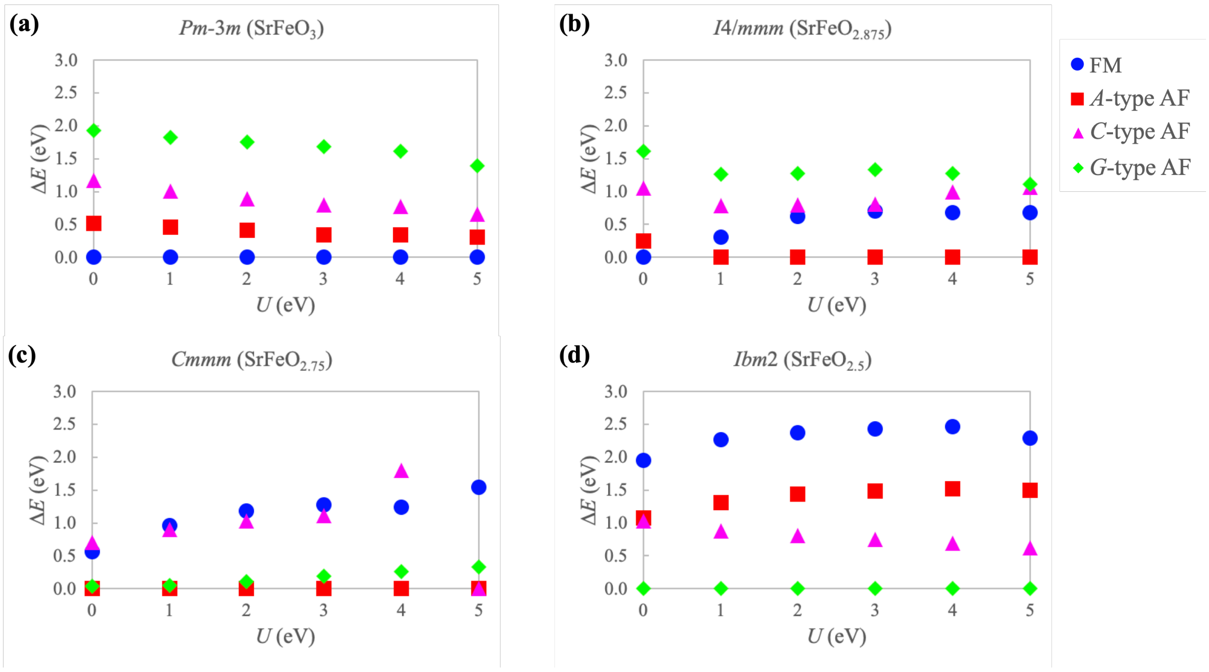

FIG. S3. Relative energy (ΔE) of (a) cubic (2×2×2) SrFeO$_3$, (b) tetragonal (2√2×2√2×2) SrFeO$_{2.875}$, (c) orthorhombic (2√2×√2×2) SrFeO$_{2.75}$, and (d) brownmillerite (√2×2√2×4) SrFeO$_{2.5}$ for various magnetic ordering as functions of U_{eff} value.

S2: Modelled crystal structures

In this section, we show how we constructed the supercells for each SrFeO$_{3-\delta}$ simulation crystal structure with respect to the cubic unit cell with the lattice parameter of a_c. The cubic supercell of SrFeO$_3$ of $Pm\text{-}\bar{3}m$ symmetry is given by (2×2×2) (Fig. S4a). For the remaining structures of SrFeO$_{3-\delta}$, with $\delta = 0.125$, 0.25, and 0.5, the crystal structure undergoes phase transformation from cubic ($Pm\text{-}\bar{3}m$) to tetragonal of $I4/mmm$ symmetry, orthorhombic of $Cmmm$ symmetry, and brownmillerite of $Ibm2$ symmetry, respectively. The tetragonal structure with 80 atomic lattice sites with two V_O's has dimension of $(2\sqrt{2}\times2\sqrt{2}\times2)$ (Fig. S4b), while the 40 atomic lattice sites of orthorhombic with two V_O's as well as brownmillerite with four V_O's have dimension of $(2\sqrt{2}\times\sqrt{2}\times2)$ and $(\sqrt{2}\times\sqrt{2}\times4)$ as shown in Fig. 4Sc and 4Sd, respectively. Each oxygen deficient crystal structure ($\delta > 0$) was rotated by 45° about c-axis with respect to the cubic unit cell.

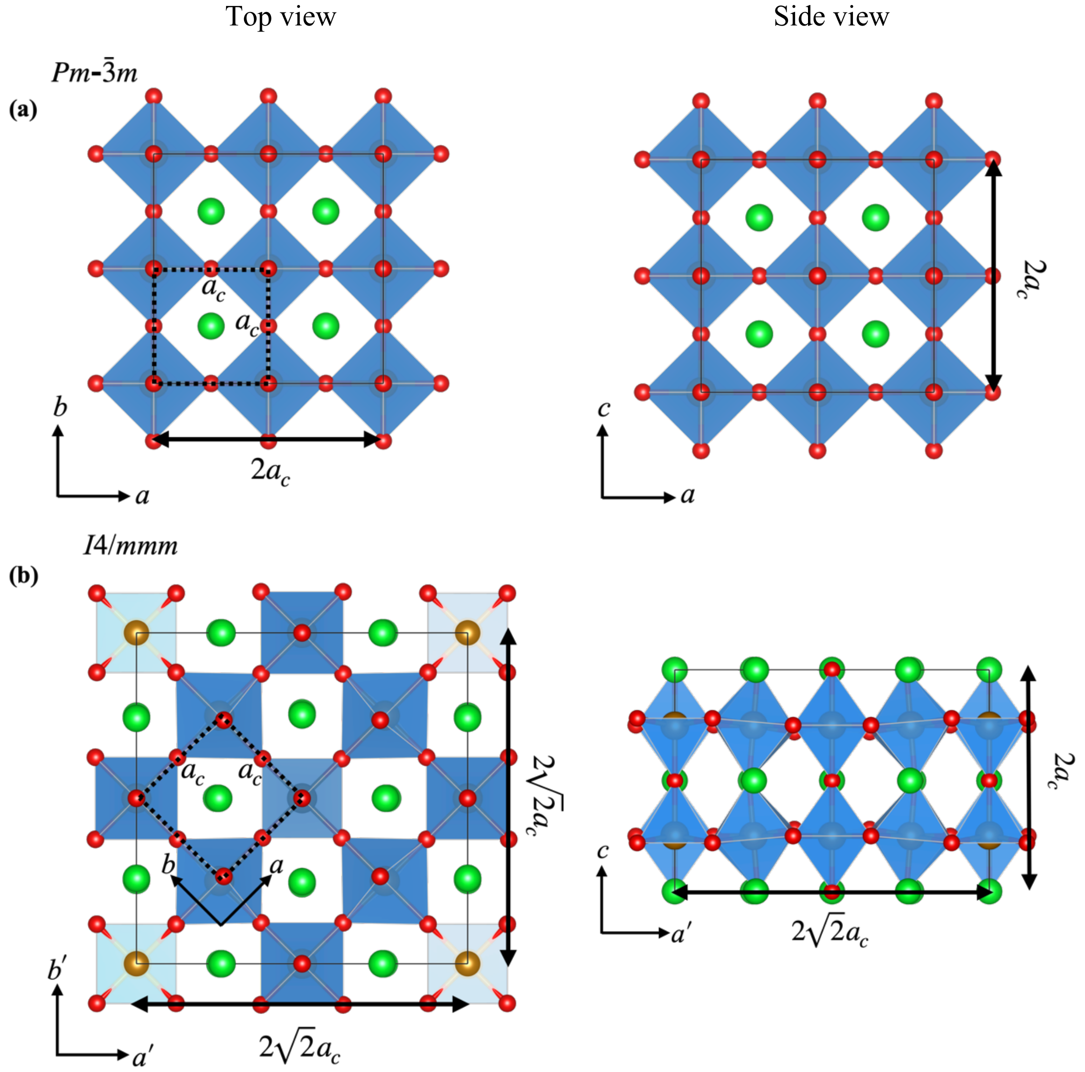

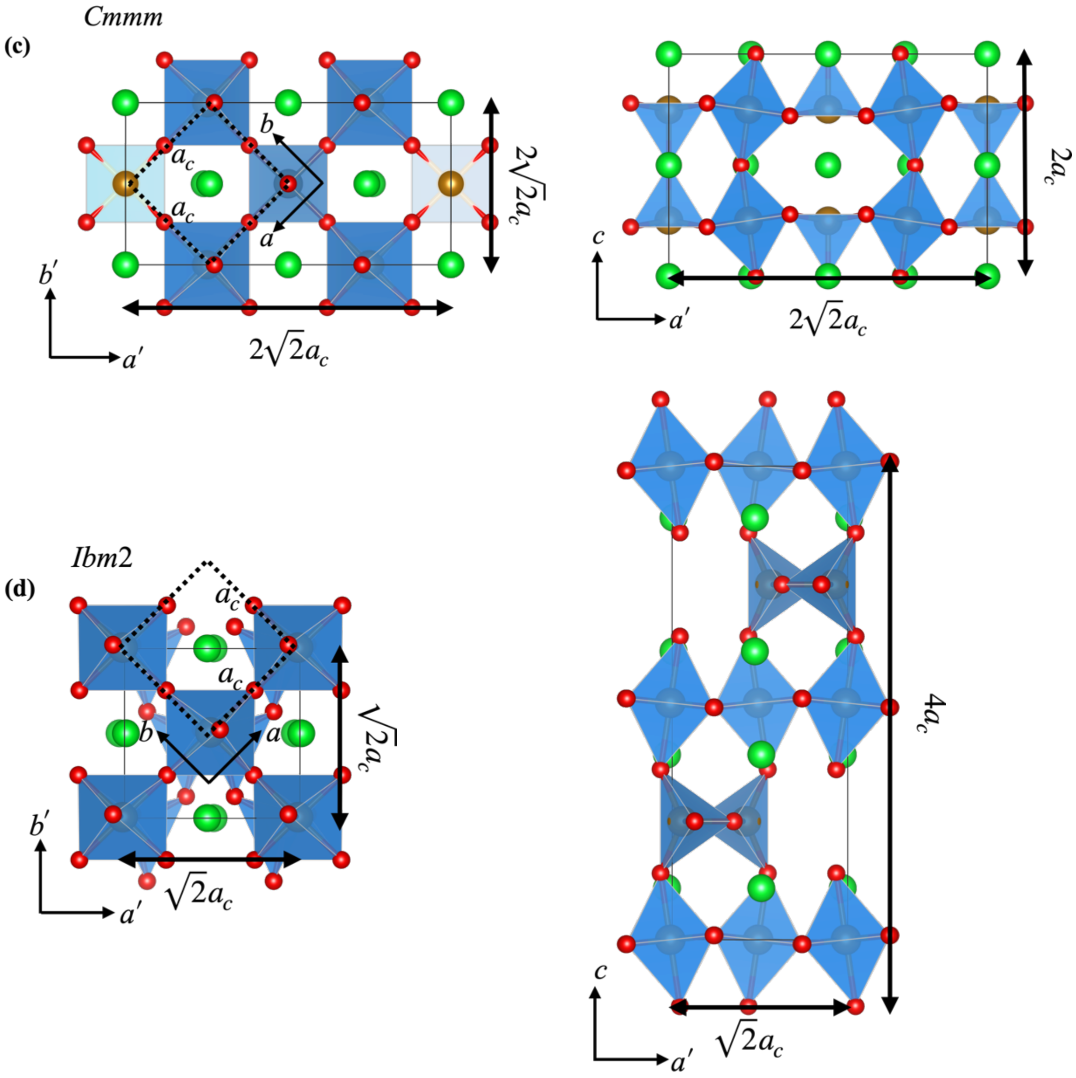

FIG. S4. Top (left) and side (right) views of the perovskite crystal structures of (a) $SrFeO_3$ cubic with the *Pm*-$\overline{3}$*m* symmetry, (b) $SrFeO_{2.875}$ tetragonal with the *I*4/*mmm* symmetry, (c) $SrFeO_{2.75}$ orthorhombic with the *Cmmm* symmetry, and (d) $SrFeO_{2.5}$ brownmillerite with *Ibm*2 symmetry. The relation between the unit cell of cubic lattice parameter a_c and the supercells of each $SrFeO_{3-\delta}$ are indicated in the figures: dotted rectangule indicates the cubic unit cell with a_c and the lattice parameters of each supercell are indicated by the arrows. In the tetragonal, orthorhombic, and brownmillerite structures, rotation by 45° about *c*-axis was imposed relative to the cubic unit cell. a' and b' axes are the rotated coordinates with respect to *a* and *b* axes of the cubic unit cell.

S3: Formation energies

We calculated the formation energy of oxygen vacancy in $SrFeO_{3-\delta}$ (ΔE^{f}_{vac}) as a function of oxygen chemical potential (μ_O) (Fig. S4) for various oxygen vacancy contents (in different supercells). We chose the lowest energy magnetic configuration for each supercells, i.e., *A*-type AF for tetragonal ($2\sqrt{2}\times2\sqrt{2}\times2$) $SrFeO_{2.875}$ and orthorhombic ($2\sqrt{2}\times\sqrt{2}\times2$) $SrFeO_{2.75}$, and *G*-type AF for brownmillerite ($\sqrt{2}\times\sqrt{2}\times4$) $SrFeO_{2.625}$ and $SrFeO_{2.5}$. ΔE^{f}_{vac} is defined by

$$\Delta E^{f}_{vac} = E(SrFeO_{3-\delta}) - E(SrFeO_3) - \frac{x}{2}E(O_2) + x\mu_O, \qquad (S4)$$

where x is the vacancy concentration, $E(X)$ is the calculated total energy of the system X. μ_O is the oxygen chemical potential as function of temperature and pressure which is given by the following expression,

$$\mu_O(T,P) = \mu_O(T,P_0) + \frac{kT}{2}\ln\left(\frac{P}{P_0}\right) \qquad (S5)$$

The zero reference state of $\mu_O(T,P)$ is half of the calculated total energy of isolated oxygen molecule, i.e., $\frac{1}{2}E(O_2)$. In Fig. S5 we plot the ΔE^{f}_{vac} at $T = 600 - 1000$ K. The trend in the ΔE^{f}_{vac} holds at various temperatures, showing that $SrFeO_{2.5}$ is the most stable phase over a wide range of oxygen chemical potentials.

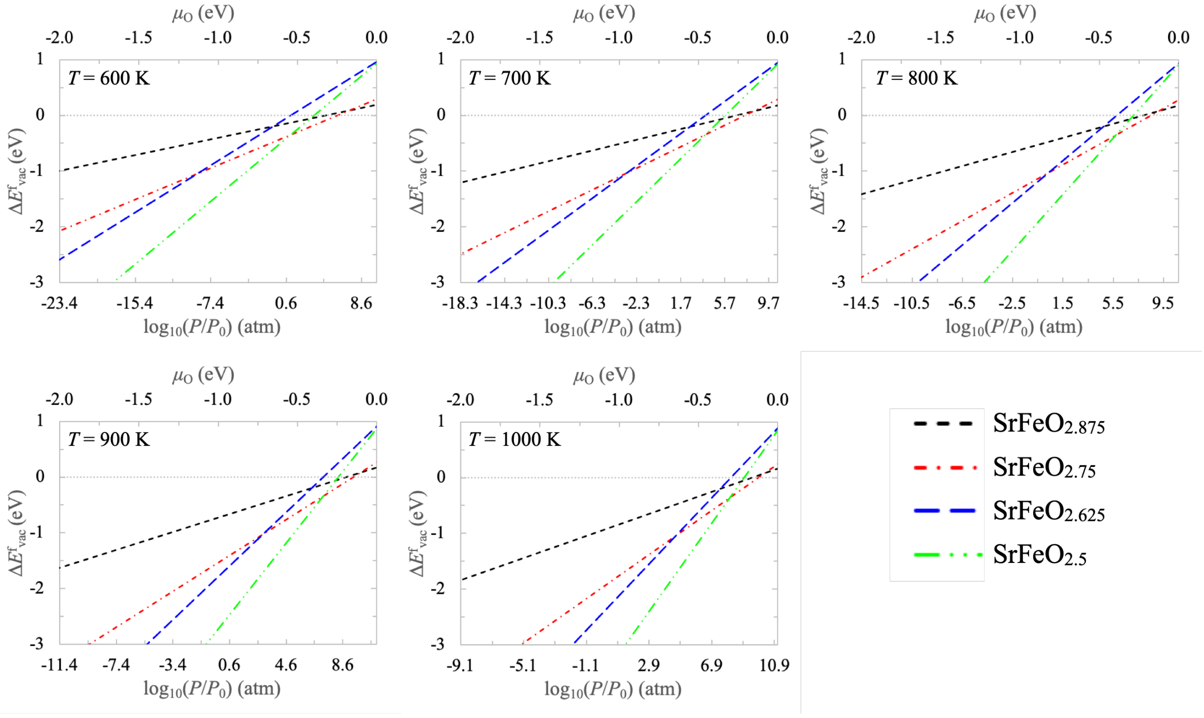

FIG. S5. Formation energies ΔE^{f}_{vac} of $SrFeO_{3-\delta}$ as a function of the oxygen chemical potential μ_O.

S4: Electronic properties

We performed the charge density difference ($\Delta\rho$) analysis in a cubic (4×4×4) supercells, in order to investigate the charge redistribution due to single V_{O} formation, i.e. $\Delta\rho = \rho(\mathrm{SrFeO_{2.98}}) + \rho(\mathrm{O}) - \rho(\mathrm{SrFeO_3})$, where $\rho(\mathrm{SrFeO_{2.98}})$, $\rho(\mathrm{O})$, and $\rho(\mathrm{SrFeO_3})$ are the total charge density of $\mathrm{SrFeO_{2.98}}$, isolated O atom, and perfect $\mathrm{SrFeO_3}$, respectively (Fig. S6). In the case of $\Delta\rho$ of the relaxed/optimized $\mathrm{SrFeO_{2.98}}$, additional O atom is added on the vacant site and the single point energy calculation was performed with further optimizing the atomic positions. In both ideal and optimized structures of cubic (4×4×4) supercells, the excess charges from the removal of single O atom are redistributed to the nearest-neighbor ions, notably to Fe@1NN and O@1NN ions. This observation supports the short-range charge redistribution mechanism in $\mathrm{SrFeO_{3-\delta}}$ systems. This mechanism also holds in smaller cubic (2×2×2) supercells of irrespective of the magnetic ordering and applied U_{eff} values, i.e. FM and *A*-type AF ordering and $U_{\mathrm{eff}} = 3$ and 4 eV, as shown in Fig. S7.

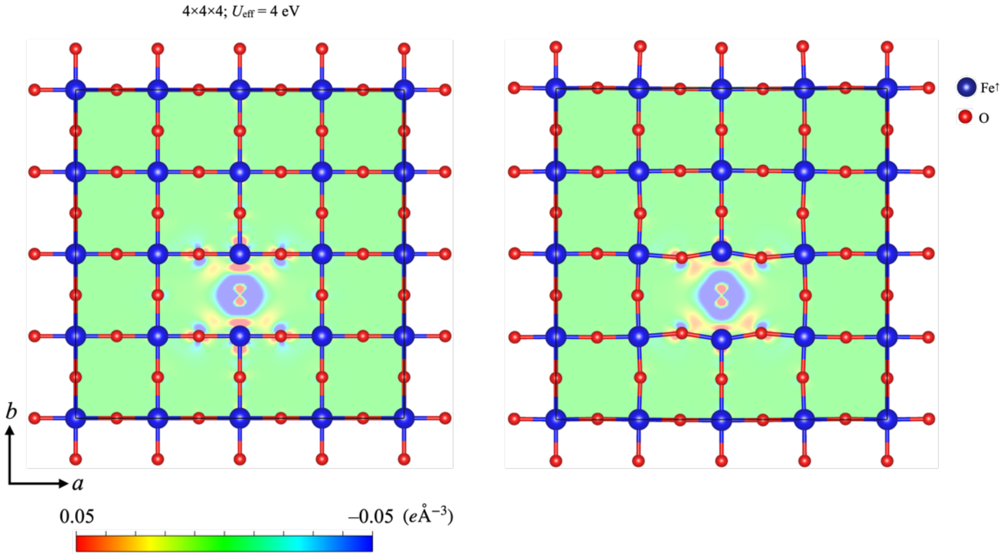

FIG. S6. Charge density difference ($\Delta\rho$) for the cubic (4×4×4) supercell of $\mathrm{SrFeO_3}$ with single O vacancy ($\mathrm{SrFeO_{2.98}}$) in ideal (left) and optimized (right) structures.

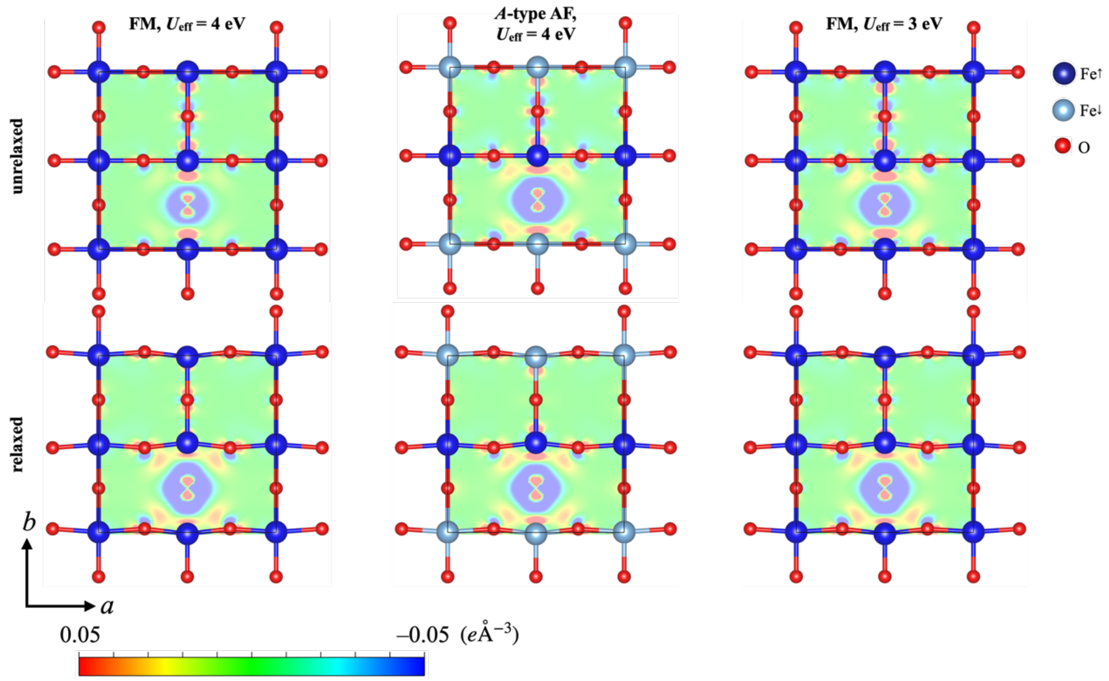

FIG. S7. Charge density difference ($\Delta\rho$) for the cubic (2×2×2) supercell of SrFeO3 with single O vacancy ($\mathrm{SrFeO_{2.875}}$) for FM ordering with $U_{\mathrm{eff}} = 4$ eV (left), *A*-type AF ordering with $U_{\mathrm{eff}} = 4$ eV (middle), and FM ordering with $U_{\mathrm{eff}} = 3$ eV (right).

Figure S8 shows the comparison of PDOS projected on to Fe ions in pristine case, Fe@1NN, and Fe@2NN in cubic (4×4×4) and (2×2×2) supercells of $SrFeO_3$ with single O vacancy obtained using different U_{eff} values. PDOSs obtained with U_{eff} of 3 and 4 eV do not show significant difference and in agreement with $\Delta\rho$ presented in Fig. S6 and S7. The profiles of Fe@2NN resembles the Fe in pristine case, while at Fe@1NN the degeneracy of e_g states are lifted and d_{z^2} states become occupied.

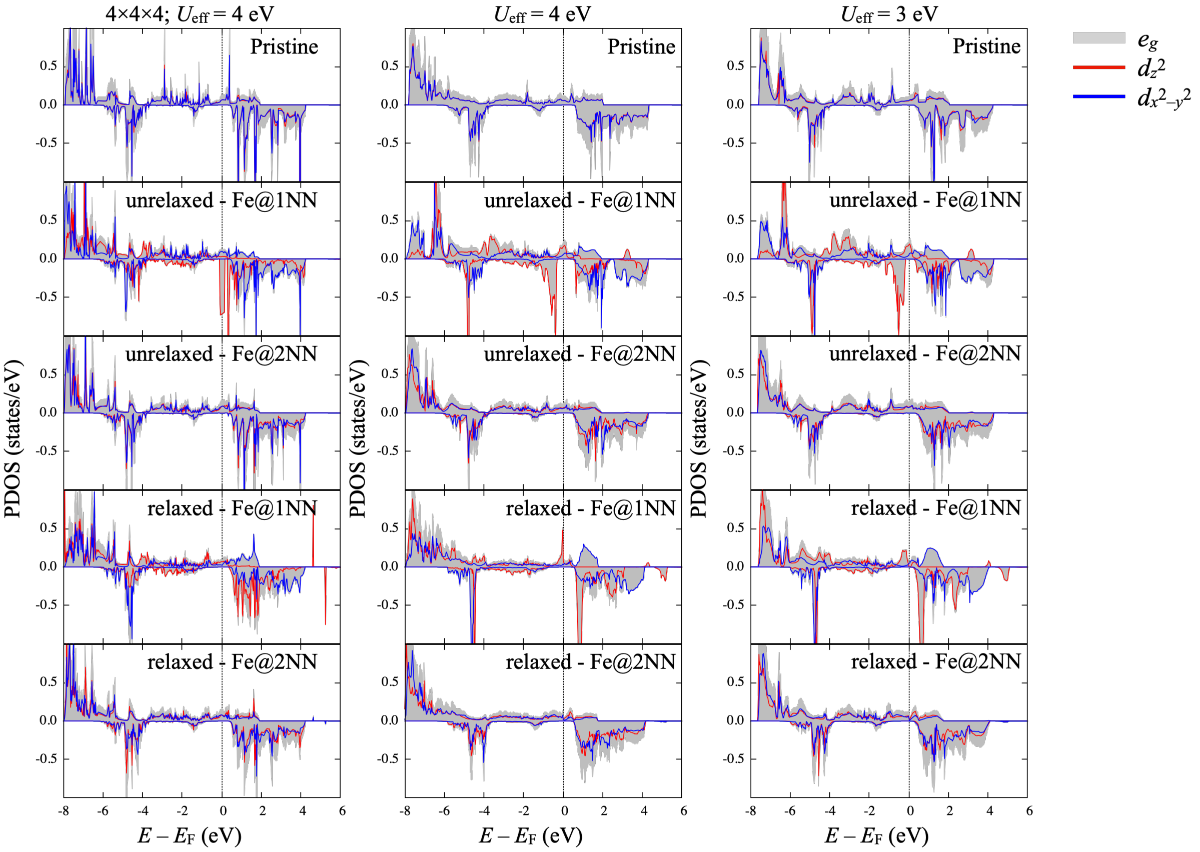

FIG. S8. Projected density of states (PDOS) for the cubic (4×4×4) supercell of $SrFeO_3$ in the FM configuration without/with single O vacancy ($SrFeO_{2.98}$) with $U_{\mathrm{eff}} = 4$ eV (left), for the cubic (2×2×2) supercell of $SrFeO_3$ in the FM configuration with and without single O vacancy ($SrFeO_{2.875}$) with $U_{\mathrm{eff}} = 4$ eV (middle), and those with $U_{\mathrm{eff}} = 3$ eV (right). The PDOSs projected onto the d_{z^2} and $d_{x^2-y^2}$ orbitals of Fe@1NN and Fe@2NN ions before and after geometry optimization are shown.

Finally, to further show the charge redistribution in $SrFeO_{3-\delta}$, we performed Maximally-Localized Wannier Functions (MLWFs) analysis as shown in Fig. S9. The localization procedure was restricted to the O_{2p} and Fe_{3d} states within −10 to 5 eV with respect to the Fermi level. As displayed in Fig. S9, MLWFs are localized in the vicinity of the V_O site and its nearest-neighbor ions, which once again support the short-range charge redistribution scenario.

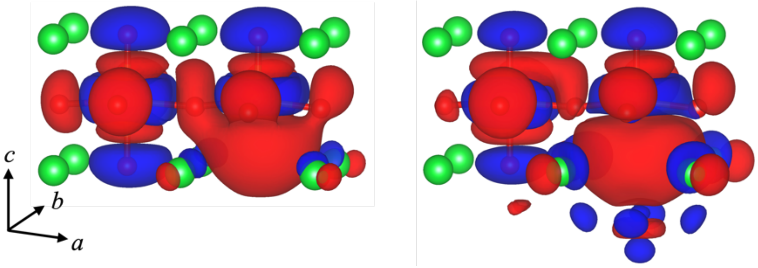

FIG. S9. Representative MLWF at Fe@1NN and Fe@2NN of (left) spin-up and (right) spin-down, calculated using the cubic $SrFeO_3$ in the (2×2×2) supercell ($SrFeO_{2.875}$). Isosurface of 0.05 eÅ^{-3}.

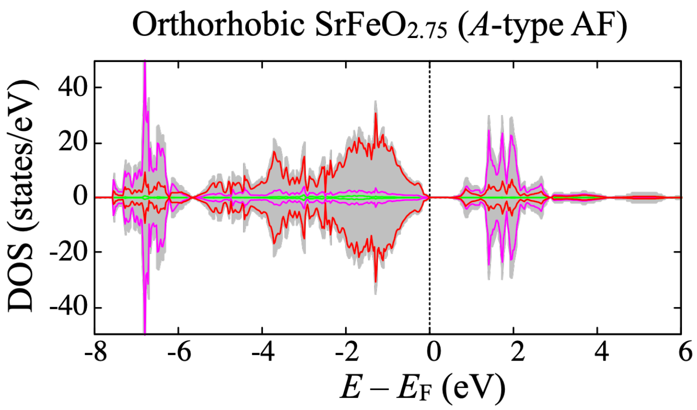
Orthorhobic $SrFeO_{2.75}$ (*A*-type AF)

FIG. S10. Density of states of *A*–type orthorhombic $SrFeO_{2.75}$.

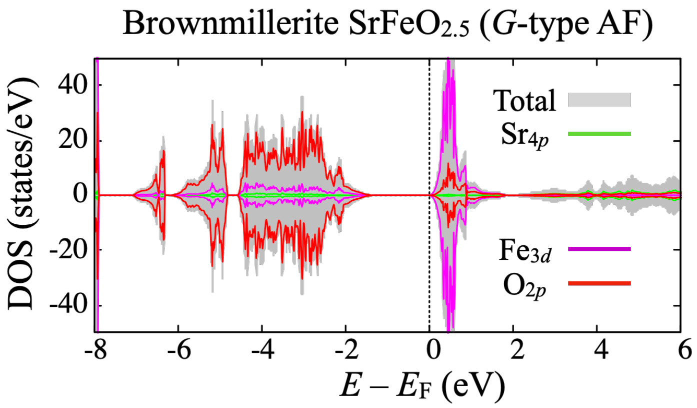
Brownmillerite $SrFeO_{2.5}$ (*G*-type AF)

FIG. S11. Density of states of *G*–type brownmillerite $SrFeO_{2.5}$.

S5: V_O–V_O interactions in $SrFeO_{2.75}$

Fig. S12 illustrate the V_O–V_O interactions in orthorhombic ($2\sqrt{2}\times\sqrt{2}\times2$) $SrFeO_{2.75}$. The overall trends in V_O–V_O configurations are hold although there is an outlier when the 2nd V_O is configured at 4NN-III with respect to the V_O^{REF}.

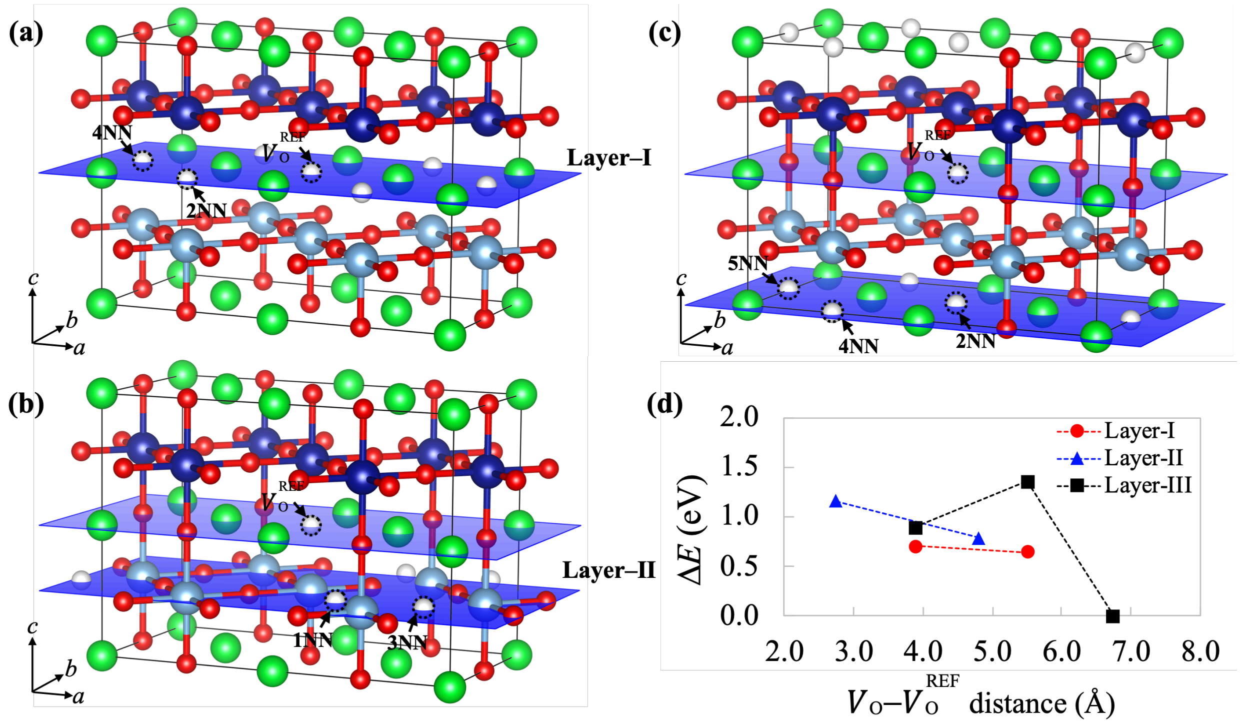

FIG. S12. (a) to (c) V_O–V_O configurations in the orthorhombic $SrFeO_{2.75}$ structure and (d) ΔE as a function of V_O–V_O distance.

S6: V_O migration

Table S1 reports the structural properties and reaction energies of the oxygen ion migration in orthorhombic (2√2×√2×2) $SrFeO_{2.75}$. The relationship between ΔE_m, $d_{Fe-O_{mig}}$, and ΔE are shown in Fig. S13. From these results we note that the mechanistic of oxygen ion migration in this orthorhombic (2√2×√2×2) $SrFeO_{2.75}$ is similar to the one in tetragonal (2√2×2√2×2) $SrFeO_{2.875}$.

Table S1. Calculated reaction energy with respect to the initial state (ΔE), Fe-O distance in the initial state ($d_{Fe-O_{mig}}$), oxygen migration path length (Δd), and migration energy for the oxygen vacancy migration (ΔE_m) of the orthorhombic $SrFeO_{2.75}$ on the *c*-direction.

Paths (Initial → Final)	ΔE (eV)	$d_{Fe-O_{mig}}$ (Å)	Δd (Å)	ΔE_m
5NN → 3NN	0.79	2.06(p)	2.59	0.99
3NN → 1NN	0.37	1.94(p)	3.77	1.11
3NN → 2NN-I	-0.08	2.02(a)	3.16	0.51
3NN → 4NN-I	-0.14	2.19(a)	3.52	0.51
3NN → 4NN-III	0.56	2.04(a)	3.69	0.94
2NN-I → 1NN	0.46	1.97(p)	3.04	0.85
2NN-I → 3NN	0.08	2.06(p)	3.16	0.60
4NN-I → 3NN	0.14	2.04(p)	3.16	0.65
3NN → 5NN	-0.79	2.11(a)	2.59	0.20

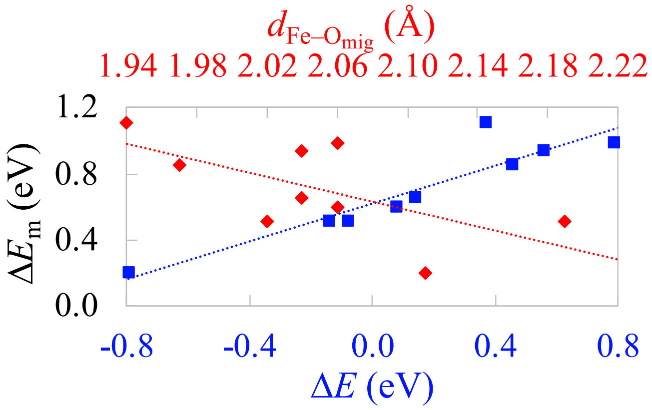

FIG. S13. ΔE_m vs ΔE and $d_{Fe-O_{mig}}$ in the orthorhombic (2√2×√2×2) $SrFeO_{2.75}$ structure.

Fig. S14 shows the migration pathways and reaction energies within the *A*-type AF orthorhombic (2√2×2√2×2) $SrFeO_{2.75}$ structure, which is twice the size (on *b*-axis) of the modelled structure describes in the main text (i.e. 2√2×√2×2). The obtained results are very close between the two different cell sizes [cf. Fig. 10 and S14], indicating that the use of smaller cell size of orthorhombic 2√2×√2×2 is reasonable.

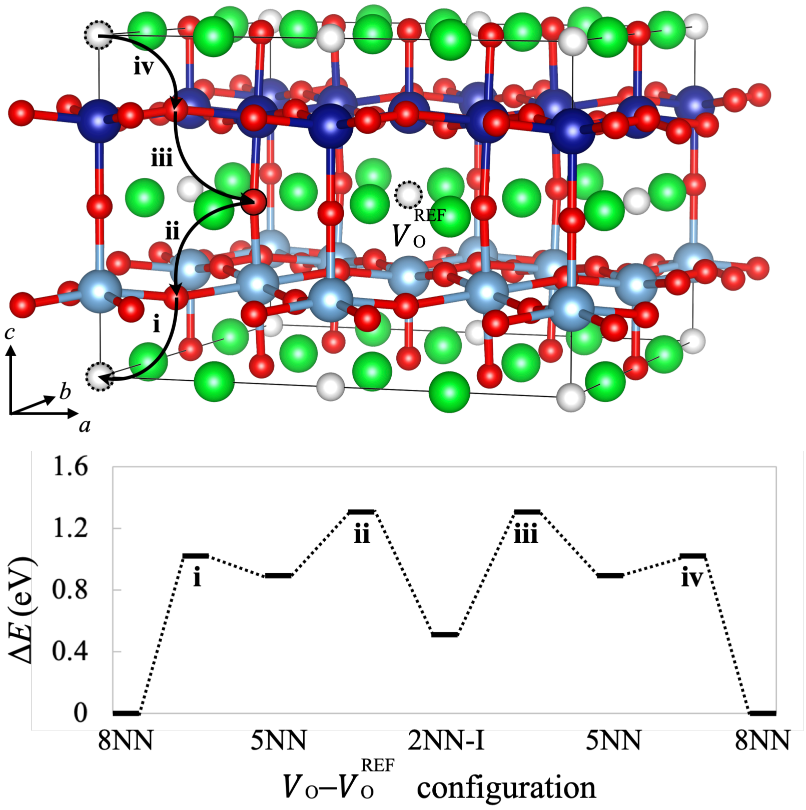

FIG. S14. (Top) The MEP within *A*-type AF orthorhombic (2√2×2√2×2) $SrFeO_{2.75}$ structure, illustrated within the structure indicated by black arrows, and (bottom) the calculated ΔE within the MEP.

Fig. S15 shows the structure of brownmillerite (2√2×2√2×4) $SrFeO_{2.531}$. The migration pathway in this particular system is through the one-dimensional vacancy channel within the tetrahedral layer. The calculated ΔE_{m} is 0.51 eV, very close to the one obtained in smaller simulation cell of brownmillerite (√2×√2×4) $SrFeO_{2.625}$. This, once again, confirms the use of smaller simulation cell size to study oxygen migration in $SrFeO_{3-\delta}$ systems.

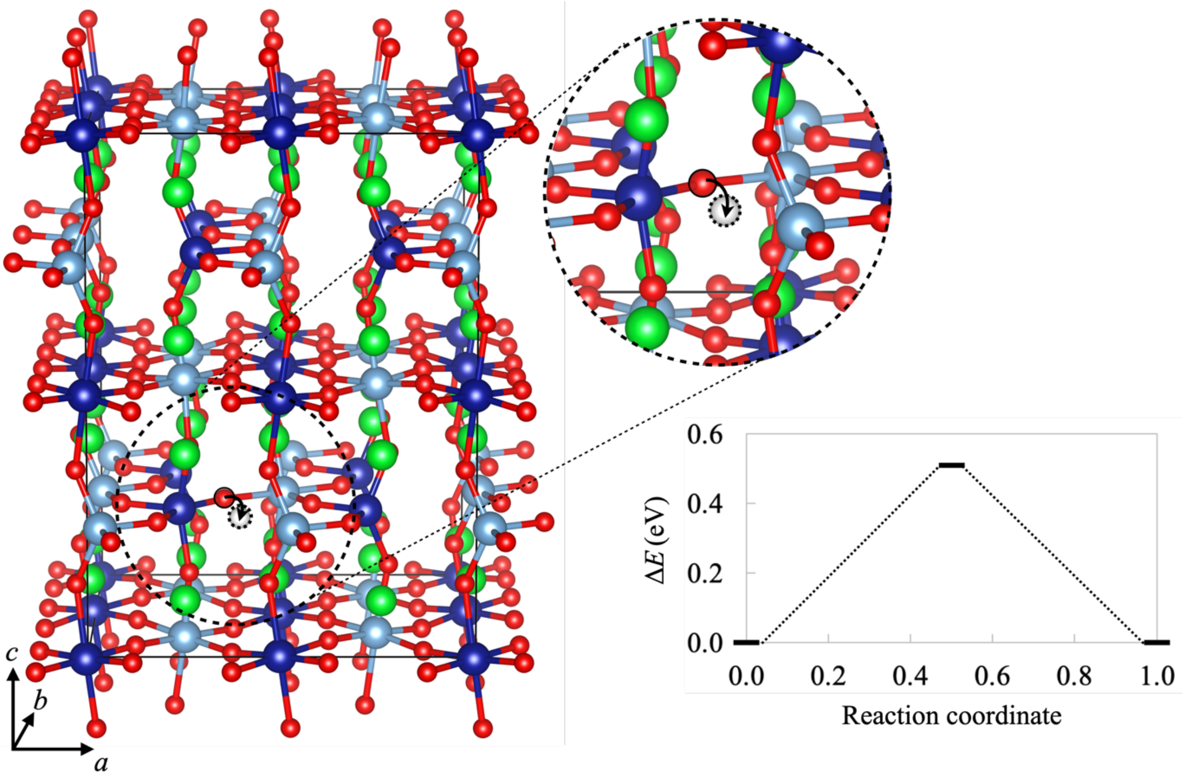

FIG. S15. The one-dimensional oxygen migration pathway in larger brownmillerite (2√2×2√2×4) structure.

Finally, Fig. S16 shows that the oxygen migration pathway in the brownmillerite SrFeO$_{2.5+x}$ systems is through one-dimensional vacancy channel due to higher migration barriers are observed along the *c*-direction: (i) 0.56 eV, and (ii) 1.55 eV.

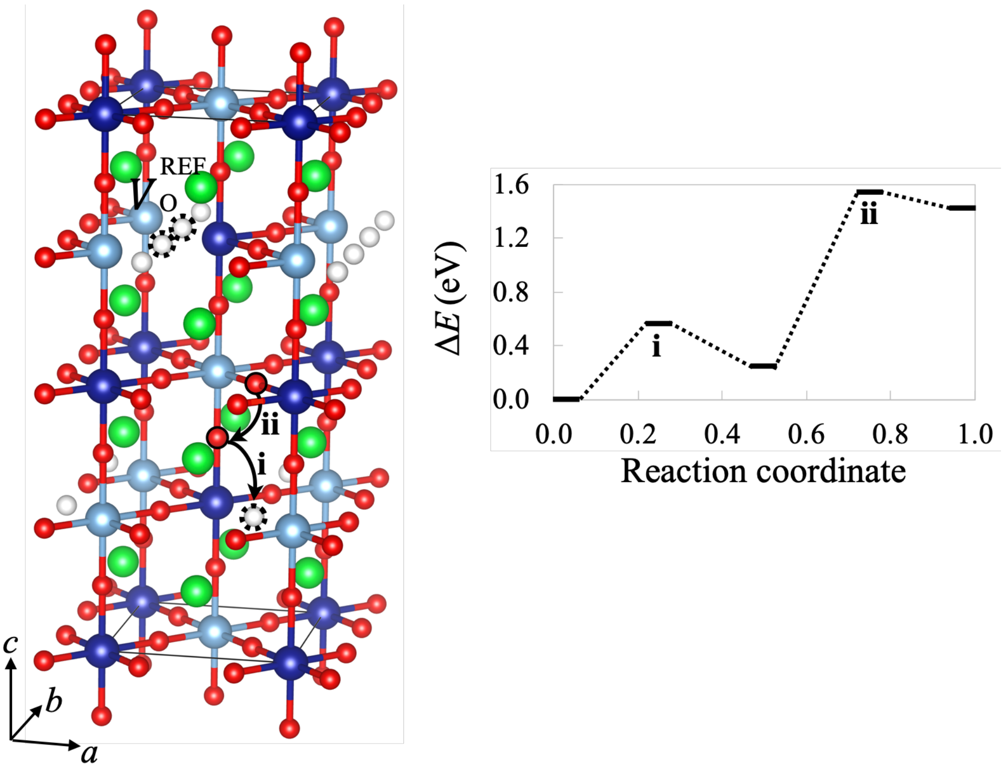

FIG. S16. ΔE in brownmillerite structure along c-direction. Other possible pathways either have even greater ΔE or the potential migrating oxygen always relaxed back to the latest configuration of “ii”, as shown in the figure, during geometry relaxations. Note that we also tried to fill one of the V_O^{REF} with the neighboring O atoms.

References

1. L. Wang, T. Maxisch and G. Ceder, *Phys. Rev. B*, 2006, **73**, 195107.
2. Y.-L. Lee, J. Kleis, J. Rossmeisl and D. Morgan, *Phys. Rev. B*, 2009, **80**, 224101.
3. *NIST Chemistry WebBook, NIST Standard Reference Database*, ed. P. J. Linstrom and W. G. Mallard, vol. 69, National Institute of Standards and Technology, Gaithersburg, 2003.
4. A. Maity, R. Dutta, B. Penkala, M. Ceretti, A. Letrouit-Lebranchu, D. Chernyshov, A. Perichon, A. Piovano, A. Bossak, M. Meven and W. Paulus, *Journal of Physics D: Applied Physics*, 2015, **48**, 504004.
5. M. Reehuis, C. Ulrich, A. Maljuk, C. Niedermayer, B. Ouladdiaf, A. Hoser, T. Hofmann and B. Keimer, *Physical Review B*, 2012, **85**, 184109.
6. J. Cheng, A. Navrotsky, X.-D. Zhou and H. U. Anderson, *Chemistry of Materials*, 2005, **17**, 2197-2207.
7. J. Vieten, B. Bulfin, M. Senholdt, M. Roeb, C. Sattler and M. Schmücker, *Solid State Ionics*, 2017, **308**, 149-155.